

# High-Performance p–n Junction Transition Metal Dichalcogenide Photovoltaic Cells Enabled by MoO<sub>x</sub> Doping and Passivation

Koosha Nassiri Nazif, Aravindh Kumar, Jiho Hong, Nayeun Lee, Raisul Islam, Connor J. McClellan, Ouri Karni, Jorik van de Groep, Tony F. Heinz, Eric Pop, Mark L. Brongersma, and Krishna C. Saraswat\*

Cite This: *Nano Lett.* 2021, 21, 3443–3450

Read Online

ACCESS |

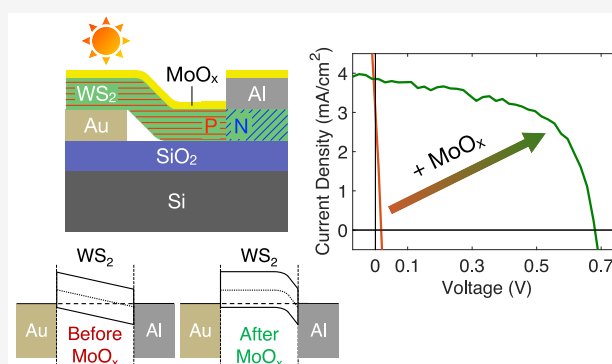
Metrics & More

Article Recommendations

Supporting Information

**ABSTRACT:** Layered semiconducting transition metal dichalcogenides (TMDs) are promising materials for high-specific-power photovoltaics due to their excellent optoelectronic properties. However, in practice, contacts to TMDs have poor charge carrier selectivity, while imperfect surfaces cause recombination, leading to a low open-circuit voltage ( $V_{OC}$ ) and therefore limited power conversion efficiency (PCE) in TMD photovoltaics. Here, we simultaneously address these fundamental issues with a simple MoO<sub>x</sub> ( $x \approx 3$ ) surface charge-transfer doping and passivation method, applying it to multilayer tungsten disulfide (WS<sub>2</sub>) Schottky-junction solar cells with initially near-zero  $V_{OC}$ . Doping and passivation turn these into lateral p–n junction photovoltaic cells with a record  $V_{OC}$  of 681 mV under AM 1.5G illumination, the highest among all p–n junction TMD solar cells with a practical design. The enhanced  $V_{OC}$  also leads to record PCE in ultrathin (<90 nm) WS<sub>2</sub> photovoltaics. This easily scalable doping and passivation scheme is expected to enable further advances in TMD electronics and optoelectronics.

**KEYWORDS:** transition metal dichalcogenides, 2D materials, tungsten disulfide, photovoltaics, molybdenum oxide, doping, passivation



The enhanced  $V_{OC}$  also leads to record PCE in ultrathin (<90 nm) WS<sub>2</sub> photovoltaics. This easily scalable doping and passivation scheme is expected to enable further advances in TMD electronics and optoelectronics.

A power supply with a high specific power (power-to-weight ratio) opens unprecedented opportunities in aerospace and transportation applications as well as wearable electronics, where lightweight yet powerful energy sources are highly desirable. Current commercial photovoltaic modules, flexible and rigid, have a specific power of less than 100 W/kg, with the exception of highly complex and expensive III–V triple junction technology, achieving >700 W/kg.<sup>1,2</sup> By adopting an ultrathin absorber material that is compatible with simple fabrication techniques and ultra-lightweight plastic packaging, 10× higher specific powers (~1000 W/kg) are achievable at a low cost.<sup>1</sup> Layered TMDs, including WS<sub>2</sub>, MoS<sub>2</sub>, WSe<sub>2</sub>, and MoSe<sub>2</sub>, are great candidates due to their excellent optical and electronic properties.<sup>3–10</sup> Semiconducting TMDs demonstrate one order of magnitude higher sunlight absorption than conventional bulk semiconductors such as GaAs and Si.<sup>6</sup> When such strong absorbers are placed in a designer multilayer stack, near-unity, broadband, and omnidirectional absorption can be achieved.<sup>11</sup> This has been demonstrated for both monolayer and multilayer TMDs in the visible spectrum.<sup>7,8</sup> The thickness-dependent bandgaps of TMDs (from ~1.0 to 2.5 eV)<sup>9</sup> cover a wide electromagnetic spectrum from visible to near-infrared regimes and are nearly ideal for single-junction or double-junction tandem photovoltaic cells.<sup>5</sup> In addition, owing to their self-passivated

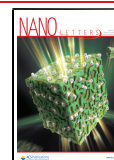
surfaces free of dangling bonds, TMDs can form heterostructures without the lattice matching constraint encountered in conventional heterostructures, offering abundant material choices for heterojunction photovoltaic cells.<sup>10</sup>

Jariwala et al.<sup>5</sup> have developed a modified Shockley–Queisser detailed balance model for TMD photovoltaic cells which uses TMDs' reported photoluminescence quantum yield (PLQY) as the upper limit of external radiative efficiency (ERE), in contrast to the original Shockley–Queisser model where ERE = 100% is assumed. According to this realistic model, one can achieve greater than 20% PCE in single-junction monolayer and multilayer TMD photovoltaic cells, provided that the external quantum efficiency (EQE) is nearly perfect, which can be enabled by optimized optical and electronic design. However, high-EQE single-junction devices reported in the literature<sup>12,13</sup> still have low PCE due to their poor carrier selectivity and defective surfaces, resulting in low open-circuit voltage ( $V_{OC}$ ). In fact, the vast majority of TMD

Received: January 3, 2021

Revised: March 29, 2021

Published: April 14, 2021



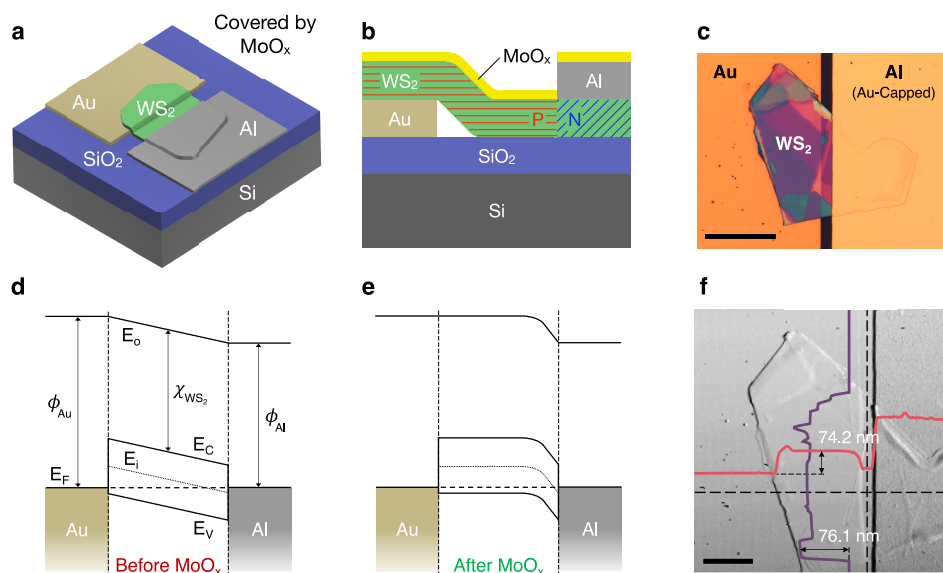


**Figure 1.** Lateral p–n junction multilayer WS<sub>2</sub> solar cells. (a) Device structure schematic. The device is covered with 5 nm of e-beam evaporated MoO<sub>x</sub> (not shown). (b) Cross-sectional view of the device. MoO<sub>x</sub> dopes the WS<sub>2</sub> p-type, creating a p–n junction near the Al top contact. Current flows diagonally through WS<sub>2</sub> from the top to the bottom contact. (c) Top-down optical image of the device. Scale bar, 20 μm. (d) Energy band diagram of initial, undoped device. The Fermi level is pinned toward the WS<sub>2</sub> midgap at the Al–WS<sub>2</sub> interface, but not at the Au–WS<sub>2</sub> interface, where the WS<sub>2</sub> is transferred gently on top. (e) Energy band diagram of p-doped device due to MoO<sub>x</sub> capping. Creating a p–n junction inside WS<sub>2</sub> significantly increases the built-in potential and V<sub>OC</sub>. E<sub>0</sub>, vacuum level; E<sub>C</sub>, conduction band edge; E<sub>V</sub>, valence band edge; E<sub>F</sub>, Fermi level; E<sub>i</sub>, intrinsic Fermi level; φ<sub>Al</sub>, Al work function; φ<sub>Au</sub>, Au work function; χ<sub>WS<sub>2</sub></sub>, electron affinity of WS<sub>2</sub>. (f) WS<sub>2</sub> thickness profiles from atomic force microscopy along dashed lines. Scale bar, 10 μm.

photovoltaic cells have V<sub>OC</sub> below 0.5 V,<sup>12–17</sup> which implies a large bandgap–V<sub>OC</sub> offset of greater than 0.8 V. Creating a high built-in potential p–n homojunction in TMDs by doping as well as passivating the surface defects would help solve this issue. MoO<sub>x</sub>, which is compatible with microelectronic processing and mass production, has been shown to be an effective, air-stable dopant for layered materials.<sup>18–21</sup> It is also known to passivate surface defects and thus reduce surface recombination.<sup>22</sup> Here, we develop an optimized MoO<sub>x</sub> charge-transfer doping and passivation method, applying it to ultrathin multilayer WS<sub>2</sub> Schottky-junction solar cells with initially near-zero V<sub>OC</sub>. These form lateral p–n homojunction devices that achieve a record high V<sub>OC</sub> of 681 mV among all p–n junction TMD solar cells with practical (i.e., nongated) designs.<sup>13–16,23,24</sup> Thanks to their high V<sub>OC</sub>, they also achieve a record PCE of 1.55% in ultrathin WS<sub>2</sub> photovoltaic cells, ~3.3 times higher than the previous record.<sup>12</sup>

We fabricate lateral p–n junction photovoltaic cells from multilayer (~20–90 nm) WS<sub>2</sub> absorber layers, electron-collecting Al top contacts (work function, φ<sub>Al</sub> ≈ 4.1 eV), and hole-collecting Au bottom contacts (φ<sub>Au</sub> ≈ 5.3 eV), with 5 nm of MoO<sub>x</sub> deposited on top for p-type charge-transfer doping and surface passivation, all sitting on a thermally oxidized silicon substrate (Figure 1a–c). The WS<sub>2</sub> layers are mechanically exfoliated from a WS<sub>2</sub> crystal and then transferred onto the Au bottom contacts using the aligned transfer method described in Supporting Information Section S1. The contacts and MoO<sub>x</sub> capping layer are deposited by electron-beam evaporation. The large work function of MoO<sub>x</sub> causes it to transfer holes into the adjacent, lower work function WS<sub>2</sub>,<sup>25</sup> leading to strong p-type doping of WS<sub>2</sub>. To improve the doping, the device is annealed at 300 °C in ambient air, which has been shown to further oxidize MoO<sub>x</sub> and therefore increase its work function.<sup>20</sup> Using this method, we achieve a

doping density of up to ~10<sup>13</sup> cm<sup>-2</sup> in WS<sub>2</sub> (see Supporting Information Section S2 for details).

Figures 1d and 1e show the energy band diagrams of our WS<sub>2</sub> photovoltaic cells before and after MoO<sub>x</sub> p-type doping. Due to interface states induced by Al top-contact evaporation, the Al Fermi level is pinned to the WS<sub>2</sub> charge neutrality level, located near the middle of the bandgap.<sup>26</sup> In contrast, there is no Fermi level pinning at the Au–WS<sub>2</sub> interface because the WS<sub>2</sub> was gently transferred onto the Au bottom contact.<sup>27</sup> The 2H phase of WS<sub>2</sub> is a weakly n-type semiconductor, with a typical charge carrier density of around 10<sup>14–15</sup> cm<sup>-3</sup> at room temperature (reported by the manufacturer), resulting in a ~2.5 μm depletion width for Au–WS<sub>2</sub> and Al–WS<sub>2</sub> Schottky junctions, fully depleting the 3-μm WS<sub>2</sub> channel between Au and Al contacts (Figure 1d). Due to Al Fermi level pinning and thus the reduced work function difference between Au and Al as well as surface recombination at the unpassivated WS<sub>2</sub> surface, this lateral Schottky-junction device is expected to produce low V<sub>OC</sub>. MoO<sub>x</sub> capping resolves this issue by creating a high-built-in-potential p–n junction inside WS<sub>2</sub> through p-type charge-transfer doping (Figure 1e) and by reducing surface recombination through passivating the surface defects. There is a possibility that a thin layer of substoichiometric AlO<sub>x</sub> is formed at the WS<sub>2</sub>–Al interface after exposure to air,<sup>28</sup> making the WS<sub>2</sub> underneath slightly more n-type.<sup>14</sup> However, this would not change the overall shape of the band diagrams in Figures 1d and 1e. Thickness profiles along the width and length of WS<sub>2</sub> channel are measured using atomic force microscopy (Figure 1f).

Using a solar simulator, we measure the current density versus voltage (J–V) characteristics of the WS<sub>2</sub> photovoltaic cells at room temperature, under global air mass AM 1.5G illumination, at various intensities before and after MoO<sub>x</sub> capping (Figures 2a and 2b). Current density is obtained by

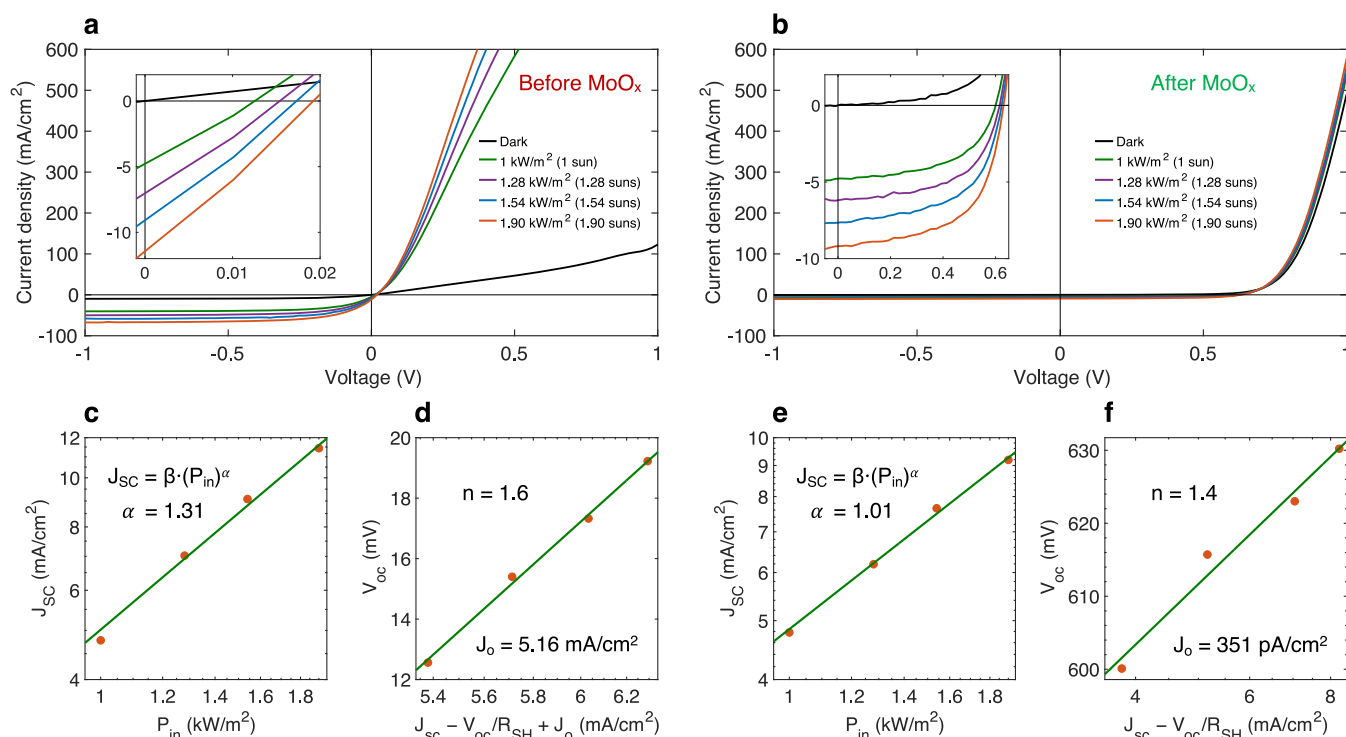


**Figure 2.** Comparison of devices before and after MoO<sub>x</sub> doping and passivation. (a, b) Power-dependent  $J$  vs  $V$  characteristics of WS<sub>2</sub> photovoltaic cells under AM 1.5G illumination (a) before and (b) after MoO<sub>x</sub> doping and passivation. Insets show a zoomed-in view of the photovoltaic region. (c)  $J_{SC}$  and (d)  $V_{OC}$  before MoO<sub>x</sub> capping. (e)  $J_{SC}$  and (f)  $V_{OC}$  after MoO<sub>x</sub> capping. Note logarithmic axes in the (c, e) plots and horizontal axis in the (d, f) plots.  $P_{in}$ , incident power;  $n$ , diode ideality factor;  $J_0$ , dark saturation current density. Symbols, measurements; lines, fits.

dividing the measured current by the device active area. Devices show rectifying behavior in both cases, and a significantly improved performance is observed after MoO<sub>x</sub> doping and passivation. Before MoO<sub>x</sub> capping, the device is a lateral Schottky-junction solar cell with a small work function difference between the two contacts and high surface recombination at the WS<sub>2</sub> unpassivated top surface, resulting in near-zero  $V_{OC}$ , as seen in Figure 2a (~12.5 mV under 1 sun illumination for the device from Figure 1). In addition, the slope of the  $J$ - $V$  curve at short circuit linearly increases with increasing incident power, which corresponds to a decreasing shunt resistance. This photoshunting effect happens in solar cells with poor carrier selectivity, where illumination leads to increased minority carrier conductivity and therefore a decreased shunt resistance.<sup>29</sup> After MoO<sub>x</sub> doping and passivation, a lateral p-n junction with high built-in potential and lower surface recombination is created between the contacts, resulting in high  $V_{OC}$ , as seen in Figure 2b (~600 mV under 1 sun illumination for the device from Figure 1). No photoshunting effect is observed in the doped p-n junction devices due to their high carrier selectivity. Also, the small slope of the  $J$ - $V$  curve at short circuit confirms the high shunt resistance associated with the Al-MoO<sub>x</sub>-Au and Al-MoO<sub>x</sub>-WS<sub>2</sub>-Au paths (if existent), which is expected due to the insulating nature of nearly stoichiometric, e-beam evaporated MoO<sub>x</sub>.

Despite doping and passivation, current density does not improve after MoO<sub>x</sub> capping (Figure 2a and 2b). This is mainly due to the suboptimal choice of the channel length. Before doping, Al-WS<sub>2</sub> and Au-WS<sub>2</sub> depletion regions cover the entirety of the channel length (Figure 1d). However, after doping, the Al-WS<sub>2</sub> depletion width is significantly decreased

(Au-WS<sub>2</sub> is now ohmic), leaving most of the channel length with no band bending and therefore poor carrier collection (Figure 1e). This is confirmed by the photocurrent map measurement discussed later in the text. Reducing the channel length would lead to channel-wide carrier collection and therefore resolve this issue.

In undoped, unpassivated devices, short-circuit current density ( $J_{SC}$ ) versus incident power ( $P_{in}$ ) follows a power law,  $J_{SC} = \beta \cdot (P_{in})^\alpha$ , with  $\alpha > 1$ , as shown in Figure 2c. This unusual superlinear behavior can be explained by the presence of intragap recombination centers with different energies and can capture cross sections.<sup>30</sup> The potential origins of these intragap states are the different WS<sub>2</sub> defect types induced during crystal growth and transfer process. These defect sites are however passivated after MoO<sub>x</sub> capping, leading to a linear  $J_{SC}$ - $P_{in}$  relationship ( $\alpha = 1$ , Figure 2e).

According to the diode eq 1, assuming that the ratio of dark saturation current density to short-circuit current density is small ( $J_0/J_{SC} \ll 1$ ) and the shunt resistance ( $R_{SH}$ ) has very large values,  $V_{OC}$  would simply scale linearly with  $\ln(J_{SC})$ , with a slope of  $nkT/q$  and the  $V_{OC}$  intercept of  $\ln(J_{SC})kT/q$ , where  $n$  is the diode ideality factor,  $T$  is the absolute temperature,  $k$  is the Boltzmann constant, and  $q$  is the elementary charge. In undoped, unpassivated WS<sub>2</sub> devices the term  $J_0/J_{SC}$  is greater than one and cannot be neglected. Also, for a more accurate ideality factor calculation, we considered the  $R_{SH}$  term in both cases. Ideality factors  $n = 1.6$  and  $1.4$  were calculated for undoped and doped WS<sub>2</sub> devices (Figure 2d and 2f), respectively, demonstrating reasonable levels of recombination in both devices, with higher recombination levels occurring in the undoped, unpassivated WS<sub>2</sub> solar cells due to their lower carrier selectivity as well as higher surface recombination.

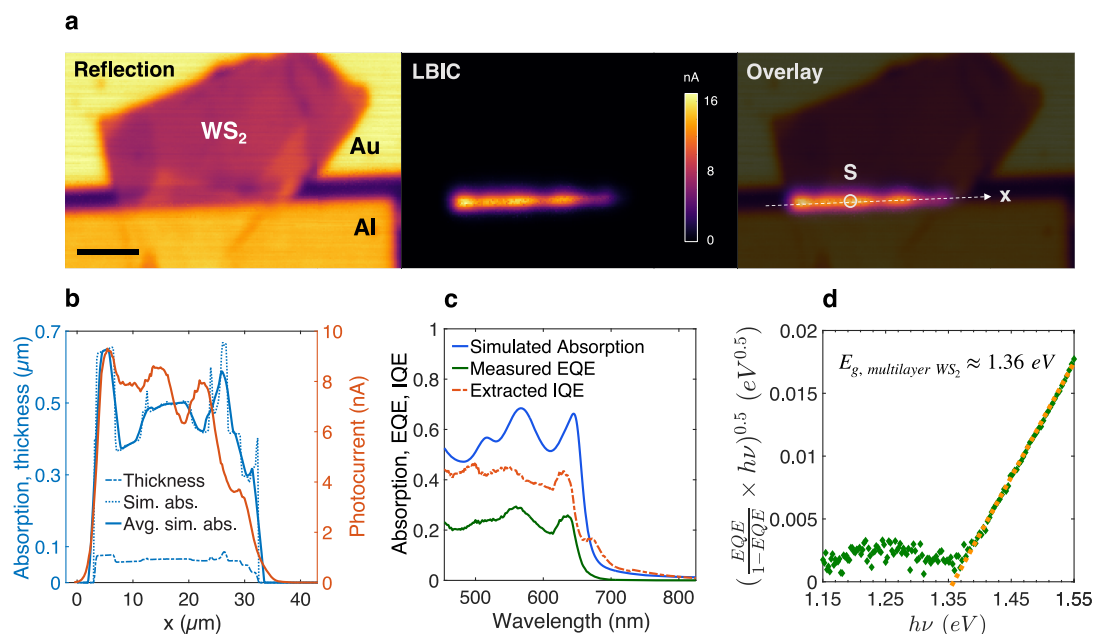


**Figure 3.** Photocurrent maps, absorption, quantum efficiency, and bandgap extraction. (a) Spatial maps of reflection, photocurrent, and reflection/photocurrent overlay for the device shown in Figure 1, measured for  $\lambda = 625$  nm. Current generation occurs only in the  $\text{WS}_2$  region located between the two contacts, which can be used to accurately define the active area of the solar cell. Scale bar,  $10 \mu\text{m}$ . (b) Measured thickness, simulated absorption (at  $\lambda = 625$  nm), and photocurrent profiles along the  $x$ -axis shown in part (a). To account for the finite laser spot size ( $\sim 2 \mu\text{m}$ ), simulated absorption at each point is also spatially averaged over its  $2\text{-}\mu\text{m}$  neighborhood on the  $x$ -axis. (c) Measured external quantum efficiency (EQE), simulated absorption, and extracted internal quantum efficiency (IQE) spectra at point S in part (a). (d) An optical bandgap of  $\sim 1.36$  eV is estimated for multilayer  $\text{WS}_2$  using the EQE data in the infrared wavelength regime, shown in Figure S3. Symbols, measurements; line, fit.

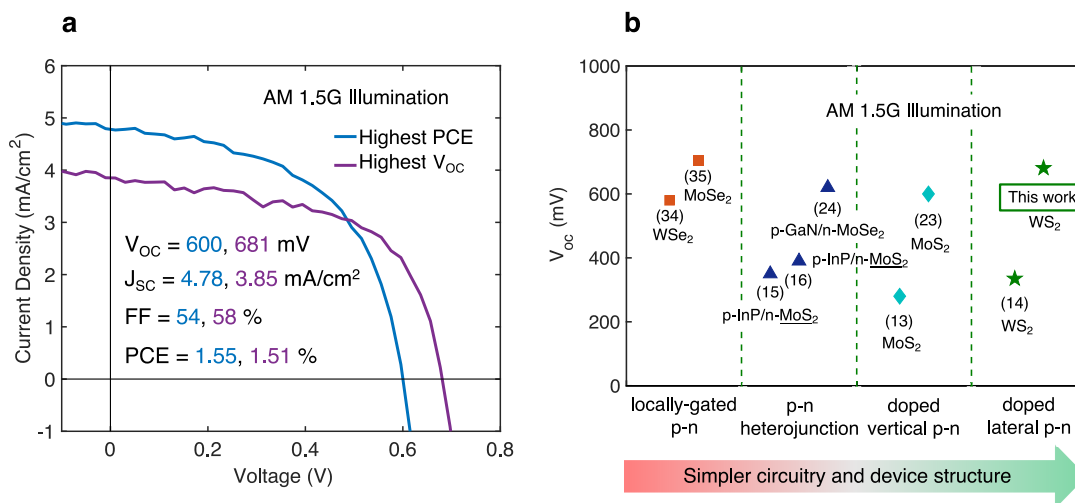


**Figure 4.** Photovoltaic performance under one-sun illumination. (a) Measured  $J$ - $V$  characteristics of two p-n junction multilayer  $\text{WS}_2$  solar cells with the highest power conversion efficiency (PCE) and  $V_{\text{OC}}$  measured using an AM 1.5G solar simulator. FF, fill factor. (b) The 681 mV  $V_{\text{OC}}$  achieved in this work benchmarked against reported  $V_{\text{OC}}$  values in the literature for TMD photovoltaic cells measured under AM 1.5G illumination. Underlined TMDs are a monolayer, and the others are a multilayer. Our one-step  $\text{MoO}_x$  doping and passivation technique represents the simplest and most manufacturable case.<sup>15–16,23,24,34,35</sup>

$$V_{\text{OC}} = \frac{nkT}{q} \ln \left( \frac{J_{\text{SC}} - \frac{V_{\text{OC}}}{R_{\text{SH}}}}{J_0} + 1 \right) \quad (1)$$

Light-beam-induced current (LBIC or, simply, photocurrent) and reflection maps concurrently acquired at a wavelength of 625 nm (Figure 3a) demonstrate that the current generation occurs only in the  $\text{WS}_2$  region located between the two contacts. Therefore, the  $\text{WS}_2$  area between

the two contacts can be used to accurately define the active area of the solar cell, which varies from  $\sim 30$  to  $\sim 360 \mu\text{m}^2$  in this work. This is, however, a nonstandard definition for the active area, suitable for small, randomly shaped TMD flakes. In traditional solar cell literature, the whole top surface of the cell is used as the active area to take into account the shading loss and series resistance associated with the top metal contact grid. For solar cells based on large-area synthesized TMD films, this standard definition should be used. The device in Figure 1,

whose  $J$ - $V$  characteristics are shown in Figure 2 and Figure 4a (blue curve), has an active area of  $92 \mu\text{m}^2$ . We observe that photocurrent is strongest at the Al- $\text{WS}_2$  junction and drastically decreases as we approach the Au- $\text{WS}_2$  junction, signaling that the channel length is too large for channel-wide carrier collection.

Measured thickness, simulated absorption (at  $\lambda = 625 \text{ nm}$ ), and photocurrent profiles along the width of the device ( $x$ -axis in Figure 3a) are plotted in Figure 3b. Absorption is simulated using the transfer matrix method. Given the finite laser spot size ( $\sim 2 \mu\text{m}$ ), simulated absorption at each point is further averaged spatially over its  $2\text{-}\mu\text{m}$  neighborhood on the  $x$ -axis. The resulting averaged absorption profile follows a similar trend to the photocurrent profile, indicating that the nonuniformity observed in the photocurrent map along the width of the device is due to thickness variations within the  $\text{WS}_2$  flake. The peak shifting seen around  $x = 25 \mu\text{m}$  can be explained by additional thickness nonuniformity perpendicular to the  $x$ -axis in that region (see Figure 1c), which affects the photocurrent map but is not taken into account in the absorption profile one-dimensional averaging.

Experimental external quantum efficiency (EQE), measured at a  $2\text{-}\mu\text{m}$ -diameter spot within the device active area (Point S in Figure 3a), along with simulated absorption and extracted internal quantum efficiency (IQE) spectra for the same spot are plotted in Figure 3c. Measured EQE and simulated absorption spectra match very well, with peaks at around wavelengths of  $565 \text{ nm}$  (reaching 30% and 68%, respectively) and  $640 \text{ nm}$  (26% and 66%) and an average of 23% and 57% over the wavelength range of  $450$  to  $650 \text{ nm}$ . This leads to a moderate internal quantum efficiency (IQE) of around 40%. Assuming EQE linearly decays to zero from  $450$  to  $0 \text{ nm}$  wavelength, we estimate  $J_{\text{SC}} \approx 5.06 \text{ mA/cm}^2$ , which is in good agreement with  $J$ - $V$  measurements under 1 sun illumination ( $J_{\text{SC}} \approx 4.78 \text{ mA/cm}^2$ ). Note that the EQE was measured at a point with higher photocurrent compared to the average observed in the active device area.

We can extract the optical bandgap ( $E_g$ ) of the absorber layer semiconductor of the photovoltaic cell by plotting the quantity  $\left(\frac{\text{EQE}}{1 - \text{EQE}} \times h\nu\right)^{0.5}$  versus the photon energy  $h\nu$ ,<sup>31</sup> where  $h$  is the Planck's constant and  $\nu$  is the photon frequency.  $E_g$  is the  $h\nu$  intercept of the line fitting the linear region of the curve. Using the infrared region of the EQE (Supporting Information Figure S3), we estimate an optical bandgap of  $1.36 \text{ eV}$  for multilayer  $\text{WS}_2$  (Figure 3d), in agreement with previously reported values.<sup>31–33</sup>

Figure 4a displays  $J$ - $V$  measurements of lateral p-n junction devices doped and passivated by  $\text{MoO}_x$ , revealing a record-breaking  $V_{\text{OC}} = 681 \text{ mV}$ , which is the highest among all nongated p-n junction TMD photovoltaic cells under AM 1.5G illumination (see benchmarking in Figure 4b). The  $V_{\text{OC}}$  improvement results in a record high PCE = 1.55% in ultrathin  $\text{WS}_2$  photovoltaic cells, 3.3 times higher than the previous 0.46% record.<sup>12</sup> A short-circuit current density  $J_{\text{SC}} = 4.78 \text{ mA/cm}^2$  is measured for the highest-PCE device, comparable to  $J_{\text{SC}}$  values observed in multilayer Schottky-junction  $\text{WS}_2$  solar cells.<sup>12</sup> The device has a shunt resistance of  $616.6 \Omega \text{ cm}^2$  and a series resistance of  $16.9 \Omega \text{ cm}^2$ , as calculated by inverting the slope of the  $J$ - $V$  curve at short-circuit and open-circuit conditions, respectively. This results in a reasonable fill factor,  $\text{FF} = 54\%$ . We measure reproducible and high  $V_{\text{OC}}$  on all six devices fabricated, ranging from  $554$  to  $681 \text{ mV}$  (Supporting

Information Figure S4). Due to thickness and thus absorption variations among the  $\text{WS}_2$  devices, as well as process variability, a range of  $J_{\text{SC}}$  and hence PCE values are observed. No hysteresis is seen in the  $J$ - $V$  curves when sweeping the voltage in the forward and backward directions (Supporting Information Figure S5). Benchmarking in Figure 4b shows that such lateral p-n junctions formed by  $\text{MoO}_x$  doping are promising for high-performance TMD photovoltaics and optoelectronics in general, especially given their simple one-step doping/passivation and device structure.<sup>13–16,23,24,34,35</sup> The compatibility of  $\text{MoO}_x$  with conventional fabrication also makes this doping and passivation technique particularly attractive for mass production.

Despite the record-breaking  $V_{\text{OC}}$  and PCE, there is significant room for performance improvement of these lateral p-n junction devices. Optical simulation using the transfer matrix method reveals that at best only about 35% of incident AM 1.5G illumination in the  $415$ – $825 \text{ nm}$  spectral range is absorbed by  $\text{WS}_2$  at thicknesses below  $100 \text{ nm}$  (see Supporting Information Section S6). Assuming unity IQE, this translates into a maximum  $J_{\text{SC}}$  of  $9.5 \text{ mA/cm}^2$ , slightly underestimated as absorption at wavelengths below  $415 \text{ nm}$  and above  $825 \text{ nm}$  are not included due to lack of material data. Adding a back reflector at the bottom of the structure is shown to significantly boost the average absorption of  $\text{WS}_2$  to  $\sim 60\%$  at thicknesses as low as  $15 \text{ nm}$ .<sup>7</sup> Switching to a vertical structure with reflective bottom metal contacts such as silver or gold is one simple way to achieve this.

Carrier collection is another area of improvement. As discussed earlier in the text, a smaller, optimal channel length would increase the band bending (lateral electric field) and therefore enhance carrier collection near the Au- $\text{WS}_2$  junction, leading to an increased  $J_{\text{SC}}$ . According to our 2D finite-element device physics simulation (see Supporting Information Section S7), there are two other sources of recombination, both due to the suboptimal design of the device structure. First, we observe that photogenerated holes travel laterally along the top surface of  $\text{WS}_2$ , next to the electron-rich  $\text{MoO}_x$  layer, before getting collected at the Au p-contact, making them highly prone to surface recombination. This is why even near the Al- $\text{WS}_2$  contact where the photocurrent is highest, about 60% of photogenerated carriers are recombined before reaching the contacts (IQE plot in Figure 3c). Reducing the channel length would alleviate this issue by decreasing the lateral distance to be traveled by photogenerated holes along the  $\text{MoO}_x$ - $\text{WS}_2$  interface. Incorporating interdigitated contacts is one way to reduce the channel length without compromising on the size of the device.

The second source of recombination is the presence of a vertical doping gradient in  $\text{WS}_2$ , resulting in electron-hole recombination near the Au contact. The doping is maximum at the  $\text{MoO}_x$ - $\text{WS}_2$  interface and decreases as we move toward the bottom surface of  $\text{WS}_2$ , leading to a vertical p-p+ junction with p and p+ regions at the wrong locations. Ideally the p+ region should be located at the p-contact (Au, bottom) to minimize electron-hole recombination nearby. Adopting a vertical structure design with Au contact at the bottom, followed by  $\text{MoO}_x$ ,  $\text{WS}_2$ , and finally the Al contact grid on top not only resolves both these carrier collection issues simultaneously but also greatly enhances absorption as mentioned earlier, unlocking higher levels of power conversion efficiency in  $\text{WS}_2$  solar cells.

In summary, we developed and optimized a simple, scalable MoO<sub>x</sub>-based doping and passivation method for TMDs, leading to record-breaking  $V_{OC}$  and PCE values when applied to ultrathin WS<sub>2</sub> solar cells. This method can be easily applied to other multilayer TMD electronics and optoelectronics, including photovoltaic cells, to create a high built-in potential p–n junction that enhances carrier selectivity and collection. Finally, we proposed guidelines to further improve the performance of the WS<sub>2</sub> devices. Together with carrier-selective contacts, light trapping schemes, and low-cost wafer-scale TMD growth methods, MoO<sub>x</sub> charge-transfer doping can lead to a game-changing TMD-based photovoltaic technology achieving greater than 20% PCE<sup>5</sup> and 1000 W/kg module-level specific power at a low cost.<sup>1</sup> Such a high-specific-power solar technology would offer unprecedented opportunities in wearable electronics, transportation, and aerospace applications of the future.

## METHODS

Devices were fabricated by first growing 90 nm of insulating SiO<sub>2</sub> on a bulk silicon wafer (resistivity of 1–4 Ω·cm) through dry thermal oxidation at 1100 °C. The wafer was then cut into 2 cm × 2 cm substrates using a wafer dicing saw (DISCO DAD3240). Next, the substrate was spin-coated by lift-off layer LOL 2000 (3000 rpm, 60 s) and subsequently baked on a 200 °C hot plate for 5 min. It was then spin-coated by Shipley 3612 photoresist (5500 rpm, 30 s) and baked on a 90 °C hot plate for 1 min. The lift-off layer/photoresist stack was later patterned using standard photolithography exposure and developing processes. Then, 40 nm of Au was deposited on top using e-beam evaporation (AJA International). After the standard lift-off process, patterned Au bottom contacts were left behind on the substrate. WS<sub>2</sub> flakes were mechanically exfoliated from the bulk crystal (2D Semiconductors) using low-residue thermal release tape (Nitto Denko REVALPHA) and then transferred onto the Au bottom contacts using the transfer method described in detail in the [Supporting Information Section S1](#). Patterned top contacts (130 nm Al/20 nm Ti/40 nm Au) were deposited using the same photolithography, e-beam evaporation, and lift-off process as the Au bottom contacts. Note that Al was coated with Au in order to avoid Al oxidation, with Ti serving as an adhesion layer between Al and Au. For the purpose of doping and passivation, 5 nm of MoO<sub>x</sub> was blanket-deposited on top by means of e-beam evaporation (Kurt J. Lesker) from a MoO<sub>3</sub> pellet (Advanced Chemicals, 99.95% purity) at a rate of 0.3 Å/s. AFM roughness analysis shows uniform deposition of MoO<sub>x</sub>. The substrate was then annealed on a 300 °C hot plate in the ambient air for 10 min to further oxidize MoO<sub>x</sub> and therefore increase its work function, leading to improved surface charge-transfer doping.

The photocurrent of the fabricated device was measured on a custom-built optoelectronic setup. A supercontinuum laser source (Fianium) was used with an acousto-optic tunable filter (Fianium) for monochromatic illumination across a broad spectral range. The laser light was modulated by a chopper wheel (400 Hz) synchronized with two lock-in amplifiers for a high signal-to-noise ratio. A 50× long working distance objective (Mitutoyo M Plan APO NIR) focused the laser light onto the sample. To image the sample with the focused laser, two beam splitters were placed in the illumination path for a halogen lamp and a CCD imaging camera, respectively. A glass slide was used to direct a small fraction of the reflected

light into a large-area Si photodiode (New Focus, model 2031) which was connected to a lock-in amplifier (Stanford Research SR810 DSP) to measure reflection from the sample. The sample was wire-bonded to a chip carrier and mounted on a three-axis piezo stage to accurately control its spatial position. Photocurrent was extracted by electrically connecting the mounted sample in series with a source meter (Keithley 2612) and a tunable current-to-voltage amplifier. The amplifier was connected to a second lock-in amplifier (Stanford Research SR810 DSP) to measure the photocurrent. To calculate EQE, the power spectrum of the incident laser was measured by a calibrated power meter (Thorlabs, PM-100USB) placed at the sample position.

A digital source meter (Keithley 2420) and a Class AAA solar simulator (Newport, Oriel Sol3A Class AAA) having a 450 W xenon short arc lamp and AM 1.5G spectral correction filter were used for AM 1.5G current–voltage measurements. The lamp was calibrated to one-sun intensity using a silicon reference cell (Newport, Oriel 91150V) placed at the location of the sample. The measurements were performed in air. The samples were kept at room temperature by means of convection cooling provided by a fan.  $J$ – $V$  curves were measured with a scan rate of 200 mV/s and a dwell time of 30 ms.

Optical simulation was performed using the transfer matrix method. We assumed a normally incident plane wave and a semi-infinite Si substrate. Optical constants for WS<sub>2</sub> and Si were taken from the literature.<sup>36,37</sup> Optical constants for MoO<sub>x</sub> were obtained experimentally from spectroscopic ellipsometry ( $n \sim 2.0$ ). SiO<sub>2</sub> was modeled as having a constant refractive index of 1.46. 2D finite-element device physics simulation was done using the COMSOL Multiphysics 5.4 semiconductor module, which solves Poisson's equation in conjunction with the continuity equations for the charge carriers. Electrical properties of WS<sub>2</sub> and MoO<sub>x</sub> were taken from the literature.<sup>12,38–40</sup> To account for illumination, a constant photogeneration rate was assumed in the WS<sub>2</sub> regions not shaded by the Al contact.

## ASSOCIATED CONTENT

### Supporting Information

The Supporting Information is available free of charge at <https://pubs.acs.org/doi/10.1021/acs.nanolett.1c00015>.

Additional details on the WS<sub>2</sub> transfer procedure, doping density estimate, EQE measurement at infrared wavelengths, reproducibility of results, forward/backward current–voltage scans showing the absence of hysteresis, thickness-dependent absorption in WS<sub>2</sub>, and 2D finite-element device physics simulation ([PDF](#))

## AUTHOR INFORMATION

### Corresponding Author

Krishna C. Saraswat – Department of Electrical Engineering and Department of Materials Science and Engineering, Stanford University, Stanford, California 94305, United States; Email: [saraswat@stanford.edu](mailto:saraswat@stanford.edu)

### Authors

Koosha Nassiri Nazif – Department of Electrical Engineering, Stanford University, Stanford, California 94305, United States; [orcid.org/0000-0002-3991-6484](https://orcid.org/0000-0002-3991-6484)

- Aravindh Kumar** – Department of Electrical Engineering, Stanford University, Stanford, California 94305, United States; [orcid.org/0000-0002-4481-9910](https://orcid.org/0000-0002-4481-9910)
- Jiho Hong** – Geballe Laboratory for Advanced Materials and Department of Materials Science and Engineering, Stanford University, Stanford, California 94305, United States
- Nayeun Lee** – Geballe Laboratory for Advanced Materials and Department of Materials Science and Engineering, Stanford University, Stanford, California 94305, United States; [orcid.org/0000-0002-9633-8000](https://orcid.org/0000-0002-9633-8000)
- Raisul Islam** – Department of Electrical Engineering, Stanford University, Stanford, California 94305, United States
- Connor J. McClellan** – Department of Electrical Engineering, Stanford University, Stanford, California 94305, United States; [orcid.org/0000-0002-8733-9968](https://orcid.org/0000-0002-8733-9968)
- Ouri Karni** – Department of Applied Physics, Stanford University, Stanford, California 94305, United States
- Jorik van de Groep** – Geballe Laboratory for Advanced Materials, Stanford University, Stanford, California 94305, United States; Institute of Physics, University of Amsterdam, 1098 XH Amsterdam, The Netherlands; [orcid.org/0000-0003-3033-8005](https://orcid.org/0000-0003-3033-8005)
- Tony F. Heinz** – Department of Applied Physics and Department of Electrical Engineering, Stanford University, Stanford, California 94305, United States; [orcid.org/0000-0003-1365-9464](https://orcid.org/0000-0003-1365-9464)
- Eric Pop** – Department of Electrical Engineering and Department of Materials Science and Engineering, Stanford University, Stanford, California 94305, United States; [orcid.org/0000-0003-0436-8534](https://orcid.org/0000-0003-0436-8534)
- Mark L. Brongersma** – Geballe Laboratory for Advanced Materials, Department of Materials Science and Engineering, and Department of Applied Physics, Stanford University, Stanford, California 94305, United States

Complete contact information is available at:

<https://pubs.acs.org/10.1021/acs.nanolett.1c00015>

### Author Contributions

K.N. and A.K. fabricated the devices, assisted by C.M. and O.K. K.N. performed the  $J$ – $V$  measurements. J.H. did the photocurrent and EQE measurements, assisted by J.G. J.H. and N.L. performed the optical simulation. K.N. carried out the 2D finite-element device physics simulation. K.N., A.K., and R.I. performed data analysis. All authors discussed the results and wrote the paper.

### Notes

The authors declare no competing financial interest.

### ACKNOWLEDGMENTS

Part of this work was performed at the Stanford Nano-fabrication Facility (SNF) and Stanford Nano Shared Facilities (SNSF), supported by the National Science Foundation under award ECCS-2026822. The authors would like to thank Isha Datye, Victoria Chen, Pranav Ramesh, and SNF staff members for their help with the fabrication process. Sample fabrication in the Heinz group was supported by the Department of Energy “Photonics at Thermodynamic Limits” Energy Frontier Research Center under grant no. DE-SC0019140. The authors acknowledge partial support from the member companies of the SystemX Alliance at Stanford.

### REFERENCES

- (1) Reese, M. O.; et al. Increasing markets and decreasing package weight for high-specific-power photovoltaics. *Nature Energy* **2018**, *3*, 1002–1012.
- (2) Cardwell, D.; Pan, N. Triple Junction GaAs High Efficiency Epitaxial Lift-Off Solar Cells. *Light, Energy and the Environment Congress 2018*, OW5C.6.
- (3) Mak, K. F.; Lee, C.; Hone, J.; Shan, J.; Heinz, T. F. Atomically thin MoS<sub>2</sub>: a new direct-gap semiconductor. *Phys. Rev. Lett.* **2010**, *105*, 136805.
- (4) Splendiani, A.; et al. Emerging photoluminescence in monolayer MoS<sub>2</sub>. *Nano Lett.* **2010**, *10*, 1271–1275.
- (5) Jariwala, D.; Davoyan, A. R.; Wong, J.; Atwater, H. A. Van der Waals materials for atomically-thin photovoltaics: promise and outlook. *ACS Photonics* **2017**, *4*, 2962–2970.
- (6) Bernardi, M.; Palumbo, M.; Grossman, J. C. Extraordinary sunlight absorption and one nanometer thick photovoltaics using two-dimensional monolayer materials. *Nano Lett.* **2013**, *13*, 3664–3670.
- (7) Jariwala, D.; et al. Near-unity absorption in van der Waals semiconductors for ultrathin optoelectronics. *Nano Lett.* **2016**, *16*, 5482–5487.
- (8) Huang, L.; et al. Atomically thin MoS<sub>2</sub> narrowband and broadband light superabsorbers. *ACS Nano* **2016**, *10*, 7493–7499.
- (9) Wang, L.; et al. 2D photovoltaic devices: progress and prospects. *Small Methods* **2018**, *2*, 1700294.
- (10) Wang, H.; et al. Two-dimensional heterostructures: fabrication, characterization, and application. *Nanoscale* **2014**, *6*, 12250–12272.
- (11) Park, J.; et al. Omnidirectional near-unity absorption in an ultrathin planar semiconductor layer on a metal substrate. *ACS Photonics* **2014**, *1*, 812–821.
- (12) Went, C. M.; et al. A new metal transfer process for van der Waals contacts to vertical Schottky-junction transition metal dichalcogenide photovoltaics. *Science Advances* **2019**, *5*, eaax6061.
- (13) Wi, S.; et al. Enhancement of photovoltaic response in multilayer MoS<sub>2</sub> induced by plasma doping. *ACS Nano* **2014**, *8*, 5270–5281.
- (14) Nassiri Nazif, K.; Kumar, A.; Moreira de Menezes, M. T.; Saraswat, K. Towards high V<sub>OC</sub>, thin film, homojunction WS<sub>2</sub> solar cells for energy harvesting applications. *Proc. SPIE, Wide Bandgap Materials, Devices, and Applications IV 2019*, 11126, 7.
- (15) Wang, P.; et al. Enhanced monolayer MoS<sub>2</sub>/InP heterostructure solar cells by graphene quantum dots. *Appl. Phys. Lett.* **2016**, *108*, 163901.
- (16) Lin, S.; et al. Gate tunable monolayer MoS<sub>2</sub>/InP heterostructure solar cells. *Appl. Phys. Lett.* **2015**, *107*, 153904.
- (17) Fontana, M.; Deppe, T.; Boyd, A.; et al. Electron-hole transport and photovoltaic effect in gated MoS<sub>2</sub> Schottky junctions. *Sci. Rep.* **2013**, *3*, 1634.
- (18) Xu, K.; Wang, Y.; Zhao, Y.; Chai, Y. Modulation doping of transition metal dichalcogenide/oxide heterostructures. *J. Mater. Chem. C* **2017**, *5*, 376–381.
- (19) Cai, L.; McClellan, C.; Pop, E.; et al. Rapid flame synthesis of atomically thin MoO<sub>3</sub> down to monolayer thickness for effective hole doping of WSe<sub>2</sub>. *Nano Lett.* **2017**, *17*, 3854–3861.
- (20) Ishikawa, R.; et al. Effect of annealing on doping of graphene with molybdenum oxide. *Appl. Phys. Express* **2018**, *11*, 045101.
- (21) Vaziri, S.; et al. Ultrahigh doping of graphene using flame-deposited MoO<sub>3</sub>. *IEEE Electron Device Lett.* **2020**, *41*, 1592–1595.
- (22) Cattin, L.; et al. MoO<sub>3</sub> surface passivation of the transparent anode in organic solar cells using ultrathin films. *J. Appl. Phys.* **2009**, *105*, 034507.
- (23) Li, H. M.; et al. Ultimate thin vertical p–n junction composed of two-dimensional layered molybdenum disulfide. *Nat. Commun.* **2015**, *6*, 6564.
- (24) Chen, Z.; et al. Wafer-size and single-crystal MoSe<sub>2</sub> atomically thin films grown on GaN substrate for light emission and harvesting. *ACS Appl. Mater. Interfaces* **2016**, *8*, 20267–20273.
- (25) Guo, Y.; Robertson, J. Origin of the high work function and high conductivity of MoO<sub>3</sub>. *Appl. Phys. Lett.* **2014**, *105*, 222110.

(26) Park, W.; et al. Complementary Unipolar  $WS_2$  Field-Effect Transistors Using Fermi-Level Depinning Layers. *Advanced Electronic Materials* **2016**, *2*, 1500278.

(27) Liu, Y.; et al. Approaching the Schottky–Mott limit in van der Waals metal–semiconductor junctions. *Nature* **2018**, *557*, 696–700.

(28) Lu, C. C.; Lin, Y. C.; Yeh, C. H.; Huang, J. C.; Chiu, P. W. High mobility flexible graphene field-effect transistors with self-healing gate dielectrics. *ACS Nano* **2012**, *6*, 4469–4474.

(29) Waldauf, C.; Scharber, M. C.; Schilinsky, P.; Hauch, J. A.; Brabec, C. J. Physics of organic bulk heterojunction devices for photovoltaic applications. *J. Appl. Phys.* **2006**, *99*, 104503.

(30) Klee, V.; et al. Superlinear Composition-Dependent Photocurrent in CVD-Grown Monolayer  $MoS_{2(1-x)}Se_{2x}$  Alloy Devices. *Nano Lett.* **2015**, *15*, 2612–2619.

(31) Kam, K. K.; Parkinson, B. A. Detailed photocurrent spectroscopy of the semiconducting group VIB transition metal dichalcogenides. *J. Phys. Chem.* **1982**, *86*, 463–467.

(32) Braga, D.; Gutiérrez Lezama, I.; Berger, H.; Morpurgo, A. F. Quantitative determination of the band gap of  $WS_2$  with ambipolar ionic liquid-gated transistors. *Nano Lett.* **2012**, *12*, 5218–5223.

(33) Arora, G.; et al. Electronic structure of layer type tungsten metal dichalcogenides  $WX_2$  ( $X = S, Se$ ) using Compton spectroscopy: Theory and experiment. *J. Alloys Compd.* **2009**, *470*, 452–460.

(34) Akama, T.; et al. Schottky solar cell using few-layered transition metal dichalcogenides toward large-scale fabrication of semitransparent and flexible power generator. *Sci. Rep.* **2017**, *7*, 11967.

(35) Memaran, S.; et al. Pronounced photovoltaic response from multilayered transition-metal dichalcogenides PN-junctions. *Nano Lett.* **2015**, *15*, 7532–7538.

(36) Li, Y.; et al. Measurement of the optical dielectric function of monolayer transition-metal dichalcogenides:  $MoS_2$ ,  $MoSe_2$ ,  $WS_2$ , and  $WSe_2$ . *Phys. Rev. B: Condens. Matter Mater. Phys.* **2014**, *90*, 205422.

(37) Palik, E. D. *Handbook of Optical Constants of Solids*; Academic Press: 1985.

(38) Meyer, J.; Kahn, A. L. Electronic structure of molybdenum-oxide films and associated charge injection mechanisms in organic devices. *J. Photonics Energy* **2011**, *1*, 011109.

(39) Dandogbessi, B. S.; Akin-Ojo, O. First principles prediction of the electronic structure and carrier mobilities of biaxially strained molybdenum trioxide ( $MoO_3$ ). *J. Appl. Phys.* **2016**, *120*, 055105.

(40) Parmendu Kant, K.; Srivastava, R. Dielectric permittivity and breakdown strength of molybdenum trioxide films. *J. Phys. Soc. Jpn.* **1975**, *39*, 1316–1318.

# Supporting Information

High-performance p-n junction transition metal dichalcogenide photovoltaic cells  
enabled by MoO<sub>x</sub> doping and passivation

Koosha Nassiri Nazif,<sup>1</sup> Aravindh Kumar,<sup>1</sup> Jiho Hong,<sup>2,3</sup> Nayeun Lee,<sup>2,3</sup> Raisul Islam,<sup>1</sup> Connor J. McClellan,<sup>1</sup> Ouri Karni,<sup>4</sup> Jorik van de Groep,<sup>2,5</sup> Tony F. Heinz,<sup>4,1</sup> Eric Pop,<sup>1,3</sup> Mark L. Brongersma,<sup>2,3,4</sup> and Krishna C. Saraswat<sup>1,3\*</sup>

<sup>1</sup>Department of Electrical Engineering, Stanford University, Stanford, CA 94305, USA

<sup>2</sup>Geballe Laboratory for Advanced Materials, Stanford University, Stanford, CA 94305, USA

<sup>3</sup>Department of Materials Science and Engineering, Stanford University, Stanford, CA 94305, USA

<sup>4</sup>Department of Applied Physics, Stanford University, Stanford, CA 94305, USA

<sup>5</sup>Institute of Physics, University of Amsterdam, 1098 XH Amsterdam, The Netherlands

\*email: [saraswat@stanford.edu](mailto:saraswat@stanford.edu)

This file includes:

- Section S1. Detailed WS<sub>2</sub> transfer procedure
- Section S2. Doping density estimate
- Section S3: EQE measurement at infrared wavelengths
- Section S4. Reproducibility
- Section S5. Forward and backward scans
- Section S6. Thickness-dependent absorption in WS<sub>2</sub>
- Section S7. 2D finite-element device physics simulation

## Section S1. Detailed WS<sub>2</sub> Transfer Procedure

Polydimethylsiloxane (PDMS, Dow Corning Sylgard™ 182) - is mixed in a glass petri dish and left in a vacuum desiccator for 48 hours to remove air bubbles and create a flat surface. PDMS is then cut into 0.5 × 0.5 cm squares with a razor blade. Each square is removed from the petri dish and placed on thin, transparent 2 × 2 cm plastic sheet. Polypropylene carbonate - PPC (Sigma-Aldrich) - was dissolved into anisole (Sigma-Aldrich) with a weight ratio of 15% PPC: 85% anisole and left on a 60°C hot plate for 24 hours in the ambient air. A drop of PCC is spin-coated on the

PDMS stamp (4000 rpm for 45 seconds). The PDMS/PPC stack is subsequently placed on a 200 °C hot plate in the ambient air for 2 minutes to further solidify PPC and improve PPC/PDMS adhesion. As shown in Fig. S1, WS<sub>2</sub> flakes are exfoliated from a WS<sub>2</sub> crystal (2D Semiconductors) using low-residue thermal release tape (Nitto Denko REVALPHA), and then picked up (exfoliated) by Gel-Film® (Gel-Pak, WF-20-X4) and transferred (exfoliated) onto the PDMS/PPC stamp. Because the WS<sub>2</sub> flake is being exfoliated with each transfer step, the outer surface of the flakes – not in contact with PPC - is clean and free of tape or Gel-Film® residue. The PDMS/PPC stamp is aligned and laminated onto the bottom contact under an optical microscope. The stage is heated to 90°C, above the transition temperature of PPC. After thermal equilibrium, the stamp is removed quickly, leaving the WS<sub>2</sub> flake behind on the substrate. The PPC residue is dissolved and removed by placing the sample in acetone for 4 minutes.

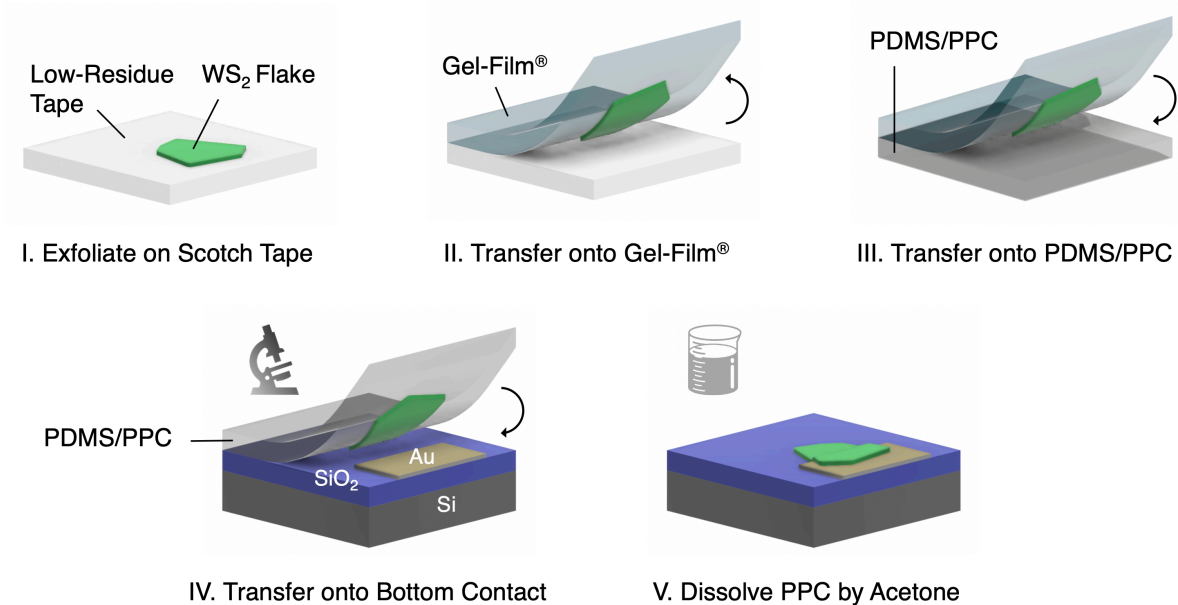


**Figure S1 | WS<sub>2</sub> Transfer Process.** (I) WS<sub>2</sub> flake is exfoliated from a WS<sub>2</sub> crystal onto a low-residue thermal release tape. The flake is (II) picked up by a Gel-Film® and then (III) transferred onto a polydimethylsiloxane (PDMS)/polypropylene carbonate (PPC) stamp. (IV) The PDMS/PPC stamp is aligned and laminated onto the bottom contact and then removed quickly above the glass transition temperature of PPC, leaving the WS<sub>2</sub> behind. (V) The PPC residue is dissolved and removed by placing the sample in acetone for 4 minutes.

## Section S2. Doping density estimate

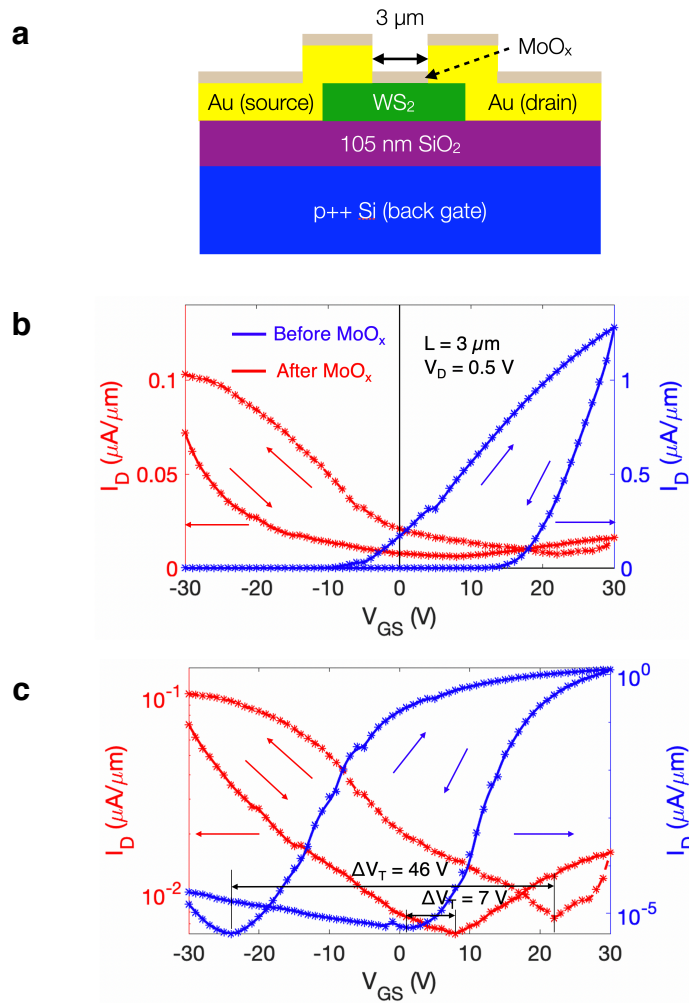


**Figure S2 | Doping density estimate.** (a) Schematic cross-section of a WS<sub>2</sub> field-effect transistor (FET) along with its (b-c) forward and reverse  $I_D$  vs.  $V_{GS}$  (drain current vs. gate voltage) sweeps measured in air, before (blue) and after (red) MoO<sub>x</sub> capping, in (b) linear and (c) logarithmic scales. Sweep directions are shown by the arrows. Device has hysteresis, due to trap states at SiO<sub>2</sub>-WS<sub>2</sub> and WS<sub>2</sub>-air interface. By passivating the trap states at the top surface of WS<sub>2</sub>, MoO<sub>x</sub> capping reduces hysteresis. The change in channel doping after MoO<sub>x</sub> capping ( $p$ ) can be estimated as  $p \approx C_{ox}\Delta V_T/q$ , where  $C_{ox} \approx 33$  nF/cm<sup>2</sup> is the gate oxide capacitance,  $\Delta V_T$  is the difference between threshold voltages before and after MoO<sub>x</sub>, and  $q$  is the elementary charge.  $\Delta V_T$  is estimated here by the difference between voltages of the transition points ( $I_D$ - $V_{GS}$  minima). A large increase in hole concentration is observed after MoO<sub>x</sub>, with a lower bound of  $1.4 \times 10^{12}$  cm<sup>-2</sup> (corresponding to  $\Delta V_T = 7$  V) and an upper bound of  $9.5 \times 10^{12}$  cm<sup>-2</sup> (corresponding to  $\Delta V_T = 46$  V).

### Section S3. EQE measurement at infrared wavelengths

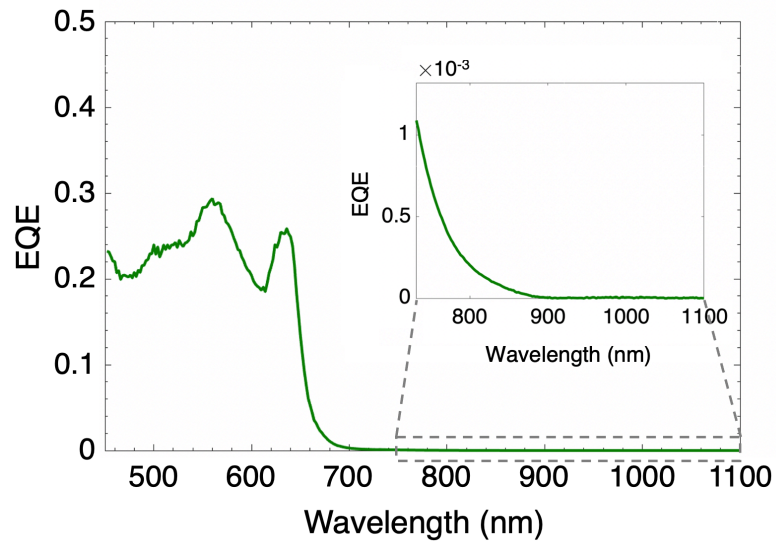


**Figure S3 | EQE measurement at infrared wavelengths.** EQE measured at a 2- $\mu\text{m}$ -diameter spot within the device active area (Point S in Fig. 3a). Inset shows a zoomed-in view of the infrared 750-1100 nm wavelength regime, which is used to extract the bandgap of multilayer  $\text{WS}_2$  (Fig. 3d).

## Section S4. Reproducibility

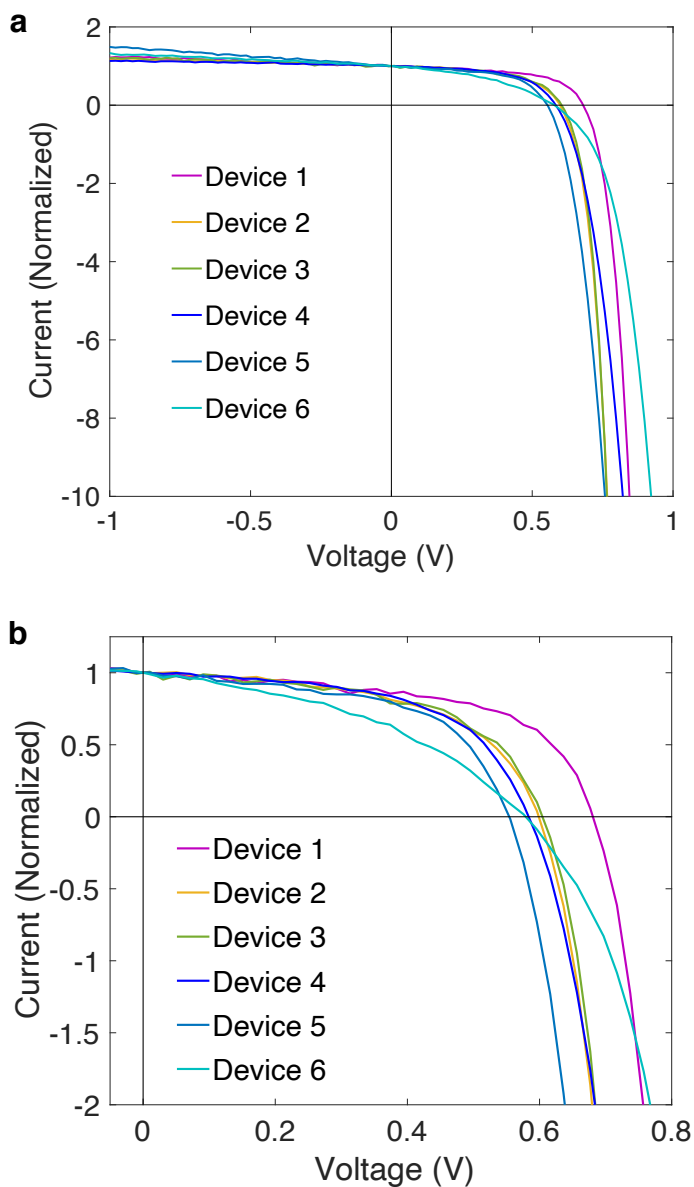


**Figure S4 I Reproducibility.** (a) I-V characteristics of 6 different devices under AM 1.5G illumination.  $V_{OC}$  is between 554 mV and 681 mV across all devices. (b) Zoomed-in view of the photovoltaic region. Current levels vary across devices due to their different thicknesses and active areas as well as process variability. For easier comparison, current is therefore normalized by the short-circuit current.

## Section S5. Forward and backward scans

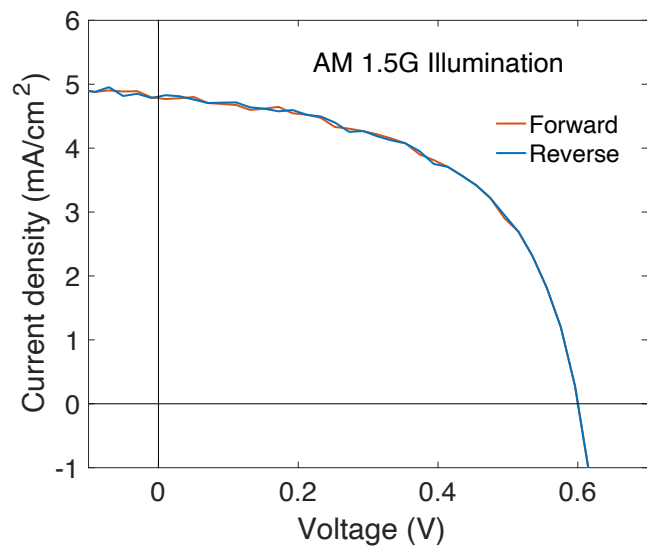


**Figure S5 | Forward and backward scans.** I-V characteristics under one-sun illumination show no hysteresis in forward/reverse voltage sweeps.

## Section S6. Thickness-dependent absorption in WS<sub>2</sub>

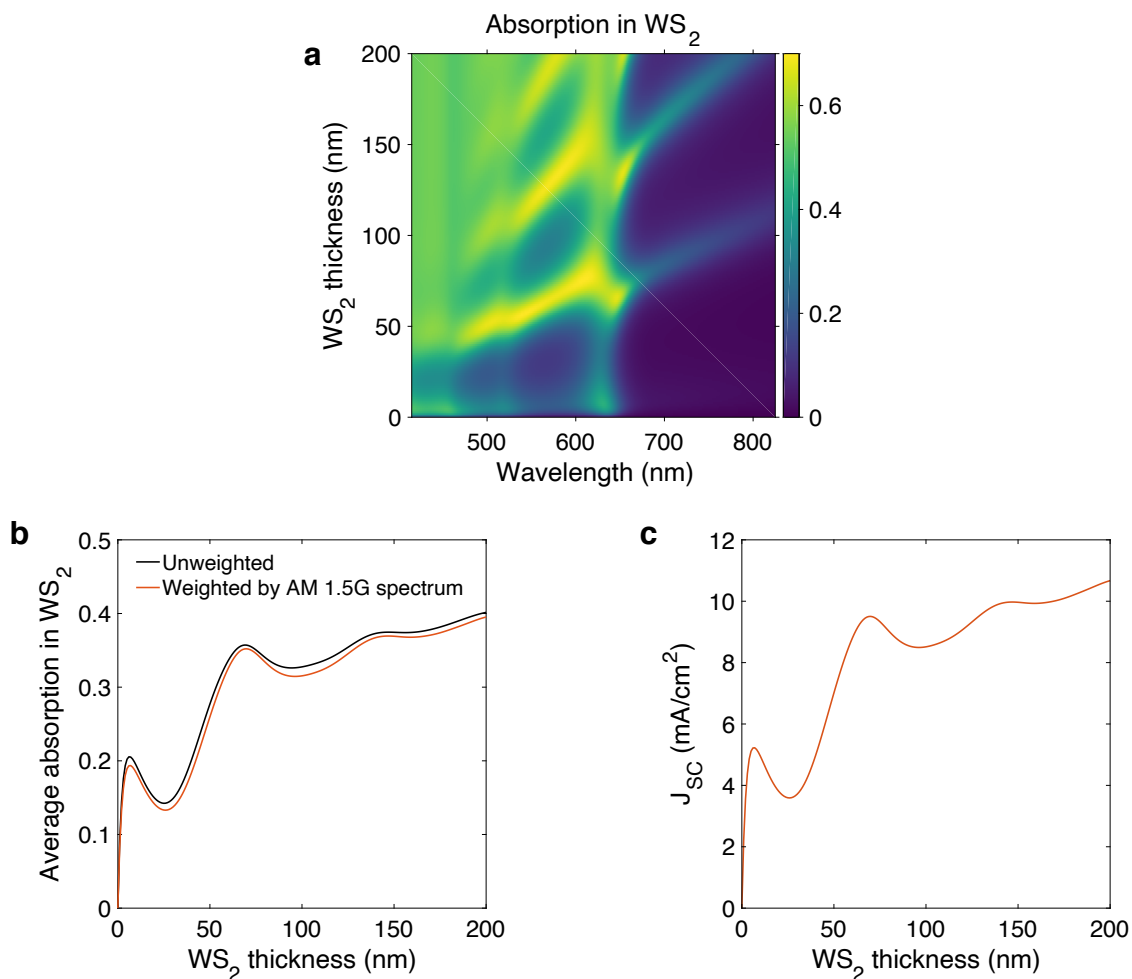


**Figure S6 I Thickness-dependent absorption in WS<sub>2</sub>.** (a) Absorption spectrum of WS<sub>2</sub> in a Si-SiO<sub>2</sub>-WS<sub>2</sub>-MoO<sub>x</sub> stack as a function of WS<sub>2</sub> thickness, simulated using the transfer matrix method. (b) Unweighted and weighted (by AM 1.5G spectrum) average of absorption in WS<sub>2</sub> as a function of WS<sub>2</sub> thickness. 70-nm-thick WS<sub>2</sub> has the highest average absorption (~35%) in the sub-100-nm thickness regime. (c) Maximum short-circuit current density (J<sub>SC</sub>) attainable from WS<sub>2</sub> in the Si-SiO<sub>2</sub>-WS<sub>2</sub>-MoO<sub>x</sub> stack as a function of WS<sub>2</sub> thickness, calculated by integrating Absorption( $\lambda$ )  $\times$  (spectral photon flux of AM1.5G spectrum at 1-sun solar intensity) over the wavelength range of  $\lambda = 415$ -825 nm, assuming unity IQE. This maximum J<sub>SC</sub> value is slightly underestimated as absorption at wavelengths below 415 nm and above 825 nm are not included due to lack of material data.

## Section S7. 2D finite-element device physics simulation

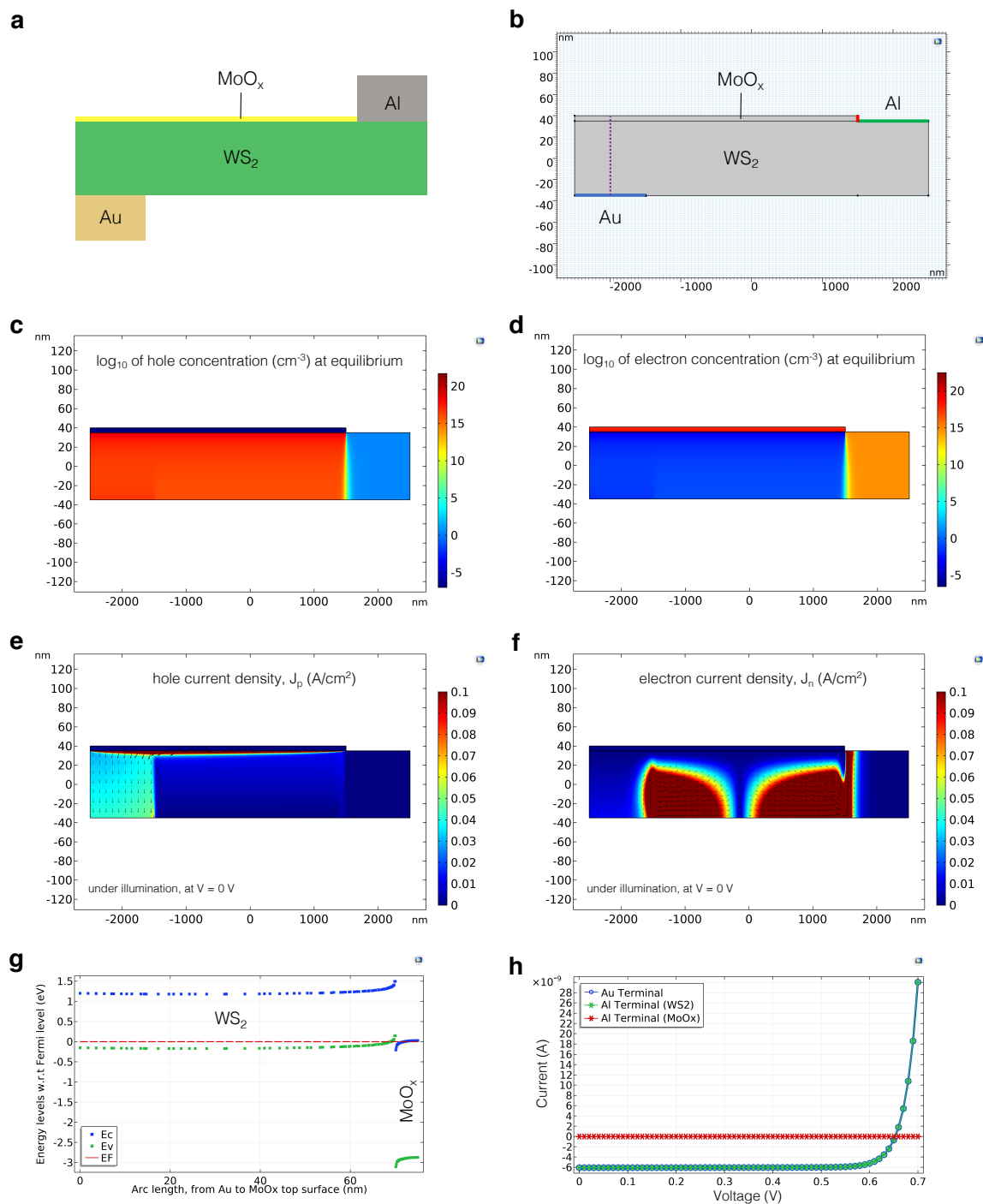


**Figure S7 | 2D finite-element device physics simulation.** (a) Schematics of the simplified device structure used in the finite-element device physics simulation study. (b) Simplified device structure simulated in COMSOL Multiphysics 5.4 semiconductor module. (c-d) Log<sub>10</sub> of (c) hole and (d) electron concentration at equilibrium, showing strong charge transfer doping of WS<sub>2</sub> by MoO<sub>x</sub>. (e-f) (e) Hole and (f) electron current density under illumination at zero applied bias.

(g) Equilibrium band diagram of the device along the purple dotted line shown in panel (b), demonstrating the vertical doping gradient in  $\text{WS}_2$ . (h) I-V curve of the simulated device under illumination, showing good agreement with the experiments. To simulate illumination, a constant photogeneration rate of  $10^{22} \text{ cm}^{-3}\cdot\text{s}$  was assumed in the  $\text{WS}_2$  regions not shaded by the Al contact. To achieve  $V_{\text{OC}} > 650 \text{ mV}$  in this simplified model, Al work functions of 4.25 eV and lower were needed. Au work function was assumed to be 5.2 eV. In conjunction with panel (e) and (f), the plot also shows that all current flows through  $\text{WS}_2$  (no conduction through  $\text{MoO}_x$ ) even if the highly electron-doped  $\text{MoO}_x$  (panel (d)) is touching the Al contact on the side. Au terminal (blue) and Al terminals contacting  $\text{WS}_2$  (green) and  $\text{MoO}_x$  (red) are highlighted in panel (b) using the same color code.